

Broad-Angle Multichannel Metagrating Diffusers

Yarden Yashno, *Student Member, IEEE*, and Ariel Epstein, *Senior Member, IEEE*

Abstract—We present a semianalytical scheme for the design of broad-angle multichannel metagratings (MG), sparse periodic arrangements of loaded conducting strips (meta-atoms), embedded in a multilayer printed circuit board configuration. By judicious choice of periodicity and angles of incidence, scattering off such a MG can be described via a multi-port network, where the input and output ports correspond to different illumination and reflection directions associated with the same set of propagating Floquet-Bloch modes. Since each of these possible scattering scenarios can be modelled analytically, constraints can be conveniently applied on the modal reflection coefficients (scattering matrix entries) to yield a diffusive response, which, when resolved, produce the required MG geometry. We show that by demanding a symmetric MG configuration, the number of independent S parameters can be dramatically reduced, enabling satisfaction of *multiple* such constraints using a *single* sparse MG. Without any full-wave optimization, this procedure results in a fabrication-ready layout of a multichannel MG, enabling retroreflection suppression and diffusive scattering from *numerous* angles of incidence *simultaneously*. This concept, verified experimentally via a five-channel prototype, offers an innovative solution to both monostatic and bistatic radar cross section reduction, avoiding design and implementation challenges associated with dense metasurfaces used for this purpose.

Index Terms—Metagratings, multichannel, multifunctionality, radar cross section, diffusers, scattering, Floquet-Bloch.

I. INTRODUCTION

THE radar cross section (RCS) of an object is a measure for the ability to detect it by the power scattered off it in a given direction when illuminated by a radar [1]. Since controlling such scattering is crucial for many defense applications, means for RCS reduction have been studied extensively over the years. The RCS depends on the respective positions of the radar antennas and the scatterer; it is customary to distinguish between bistatic radar scenarios, where the transmitter and receiver are separated by a distance comparable to their distance to the target, and monostatic radar scenarios, where the transmitter and receiver are co-located. While in the former case, the angle of incidence upon the target generally differs from the reflection angle that would be intercepted by the receiver, in the latter, the detection is based on the retroreflection from the target. Therefore, and considering that the angle of illumination is unknown in general, the ideal RCS reduction cover would need to diminish scattered fields in as many directions as possible, and perform equally well for multiple excitation scenarios.

In recent years, metasurfaces (MS), thin sheets of closely-packed subwavelength polarizable particles (meta-atoms), have

been extensively investigated as means to tackle such challenges [2]. Being low-profile and conformal, and with their proven ability to control wave scattering for various applications, they have the potential to serve as effective target coatings, acting to reduce their radar signature. One approach to achieve this is to design absorbing MSs [3], [4], which could be used to suppress both monostatic and bistatic RCS at the same time. However, such devices require engineering lossy materials within thin sheets, which is often nontrivial from a practical standpoint [5].

Alternatively, one can avoid such complexities while still obtaining substantial RCS reduction with ultrathin covers by using diffusive MSs. One such common design relies on the checkerboard configuration, as proposed in [6]–[8]. These structures are composed of alternating perfect electric conductor (PEC) and artificial magnetic conductor (AMC) reflective unit cells; when excited by a normally incident plane wave, the π phase shift between the PEC and AMC reflected waves cause destructive interference in that direction. While these surfaces are relatively simple to design and manufacture, they aim to reduce the monostatic RCS for normal-direction excitation scenarios (where the specular reflection coincides with the retroreflection), yet expose the target for detection from other angles.

An evolution of this idea, presented in [9]–[15], uses diffusive metasurfaces composed of elements exhibiting varying reflection phases, thereby purposely deflecting the specular reflection towards (one or more) different directions. However, since the reflection phases correspond to normally incident wave excitations, wide-angle response is generally not guaranteed. Extending the angular response is typically obtained via brute-force optimization methods, not as an inherent part of the design, which is usually time consuming and lacks physical insight [5].

Further to the challenges described in the previous paragraphs, utilizing MSs for RCS reduction faces an additional, more fundamental difficulty, resulting from the need to obey the homogenization approximation. To form the equivalent surface constituents¹ yielding the generalized sheet transition conditions (GSTC) governing most of the synthesis procedures [16], dense closely-packed meta-atom arrangements should be used. Such a requirement, however, tends to complicate the design and fabrication processes due to the need to devise and realize a large number of particles with deep subwavelength features and small separation distances. In addition, following the typical GSTC-oriented synthesis approach results in abstract MS constituent distribution, which generally implements

The authors are with the Andrew and Erna Viterbi Faculty of Electrical and Computer Engineering, Technion - Israel Institute of Technology, Haifa 3200003, Israel (e-mail: epsteina@ee.technion.ac.il).

Manuscript received August XX, 2022; revised ***, **, ****.

¹In the aforementioned [6]–[15], these constituents are effectively the local reflection coefficient magnitudes and phases.

the desired surface response for a given (single) excitation² [17]. Thus, even if one succeeds translating these constituents into a practical MS prototype, usually via full-wave simulations utilized to design the physical geometries associated with the various meta-atoms, attributing multifunctional properties to the MS (e.g., accommodating multiple angles of incidence) forms yet another nontrivial challenge.

To address these issues, we present herein an alternative approach, utilizing the concept of metagratings (MG) to devise effective diffusive covers with broad acceptance angle. Similar to MSs, MGs are composed of small polarizable elements, arranged periodically; however, in contrast to MSs, the meta-atoms in MGs are sparsely distributed [18]. Due to their sparsity, MGs are not governed by homogenization; instead, to design them, the detailed interactions between the meta-atoms are considered based on a suitable analytical model, tying the available geometrical degrees of freedom (DOF) to the scattered fields. Subsequently, by judicious tailoring of the meta-atom distribution and their detailed dimensions, the scattering from individual elements can be engineered to form a desired interference pattern. This yields efficient high-fidelity practical designs, avoiding the extensive full-wave optimization associated with MS synthesis while featuring simpler and easier-to-fabricate layouts [19]–[22].

Indeed, in recent years, we have developed a semianalytical scheme to synthesize multilayer printed-circuit-board (PCB) MGs based on capacitively-loaded conducting wires as meta-atoms [Fig. 1(a)–(c)], demonstrating the ability to manipulate beams at microwave frequencies in versatile manners with high efficiencies [23]–[27]. Similar configurations have been subsequently used in a wide variety of scenarios, allowing diverse static and dynamic beamforming [28]–[32], enhancing waveguide systems [33], [34], and alternative antenna devices [35]–[37].

To harness this concept to obtain broad-angle reduction of both monostatic and bistatic RCS, we utilize a multichannel scattering perspective [38], [39]. Since MGs are periodic composites, they must comply with the Floquet-Bloch (FB) theorem. In other words, when illuminated by a plane wave, real power can only be scattered into a finite set of discrete directions (associated with the various FB modes), determined by the angle of incidence and the period length. Accordingly, we describe the MG as a multiport network, where the input and output channels are defined by the angles of incidence and the corresponding scattering angles, respectively [38], [40] [Fig. 1(a)]. We leverage this method to design a MG, which for *each* excitation scenario, evenly scatters the incident power between the output channels, while specifically suppressing the coupling to the retroreflection channel [Fig. 1(d)]; thus, wide-angle monostatic and bistatic RCS reduction is achieved within a single passive device.

Specifically, to design a suitable multielement multilayer MG, we harness the model presented in [23], [24], [26], invoking first the superposition principle to evaluate separately the scattering off the given PCB dielectric stack in the absence

of the MG grid (external fields), and the contribution of the secondary fields produced by the currents induced on the MG [20], [41]. Next, we utilize Ohm's law to relate these currents to the electric fields acting on the loaded wires, forming a set of coupled equations associating the MG properties (wire positions and capacitive loads) with the induced currents and overall FB coupling coefficients. This analytical formulation, in turn, can be used to evaluate the scattered fields for given MG configuration and incident beam angle (the forward problem), serving as the basis for the inverse problem solution: retrieving the meta-atom constellation and dimensions that would generate the desired interference patterns when illuminated from *each* of the *multiple* considered excitation angles (input channels)³.

Importantly, by formulating the desired scattering requirements for the possible angles of incidence as a set of constraints imposed on the structure's scattering matrix (S-matrix), it is possible to evaluate and possibly reduce the number of DOFs needed to realize the multifunctional MG. In general, since we strive to devise a passive and lossless design, reciprocity and power conservation are enforced, identifying the minimal set of independent scattering coefficients. However, herein we impose an additional requirement, demanding that the MG configuration would be symmetric. Aligned with the broad-angle RCS reduction scenario, we show that such a symmetry requirement also reduces the number of overall independent S-parameters, translated into a reduced number of constraints. In contrast to other recently reported multifunctional MG designs, e.g. [32], [42], [43], this symmetry-oriented approach we follow allows dramatic minimization of the required elements per period, leading to a compact and sparse formations. This methodology, verified via full-wave simulations and demonstrated experimentally, yields a general and reliable approach for designing multichannel MGs for versatile and broad angle beam-manipulation applications. In particular, it paves the path to enhanced low-profile RCS reduction covers, which are simple to fabricate (sparse) and design (require no full-wave optimization), successfully suppressing both monostatic and bistatic RCS for multiple angles of incidence.

II. THEORY

A. Scattering off a PCB MG (analysis)

We consider a 2D ($\partial/\partial x = 0$) Λ -periodic structure, composed of N metallization layers embedded in a dielectric substrate of permittivity $\varepsilon_2 = \varepsilon_{\text{sub}}$ bounded within the region $z \in [0, t_N]$, backed by a PEC at $z = t_N$ and surrounded by a medium (air, by default) with permittivity ε_1 occupying the half-space $z < 0$ [Fig. 1(a)]. The wavenumbers and

³As will be laid out in detail in Section II, this design methodology differs from the one employed in [23], [24], [26], where effectively only the wire coordinates were used directly as DOFs for the synthesis process, and the load impedances were set automatically once these were determined as to satisfy the linear set of constraints on the coupling coefficients (*cf.* Eqs. (17)–(20) of [26]). Herein, we use both the load impedances and the wire coordinates as independent DOFs and rely on inverse solution of the overall (nonlinear) set of constraints (taking into account also multiple excitations), which is essential for achieving the multichannel functionality with a minimal number of meta-atoms per period.

²The designated excitation is typically a normally incident plane wave [6]–[15].

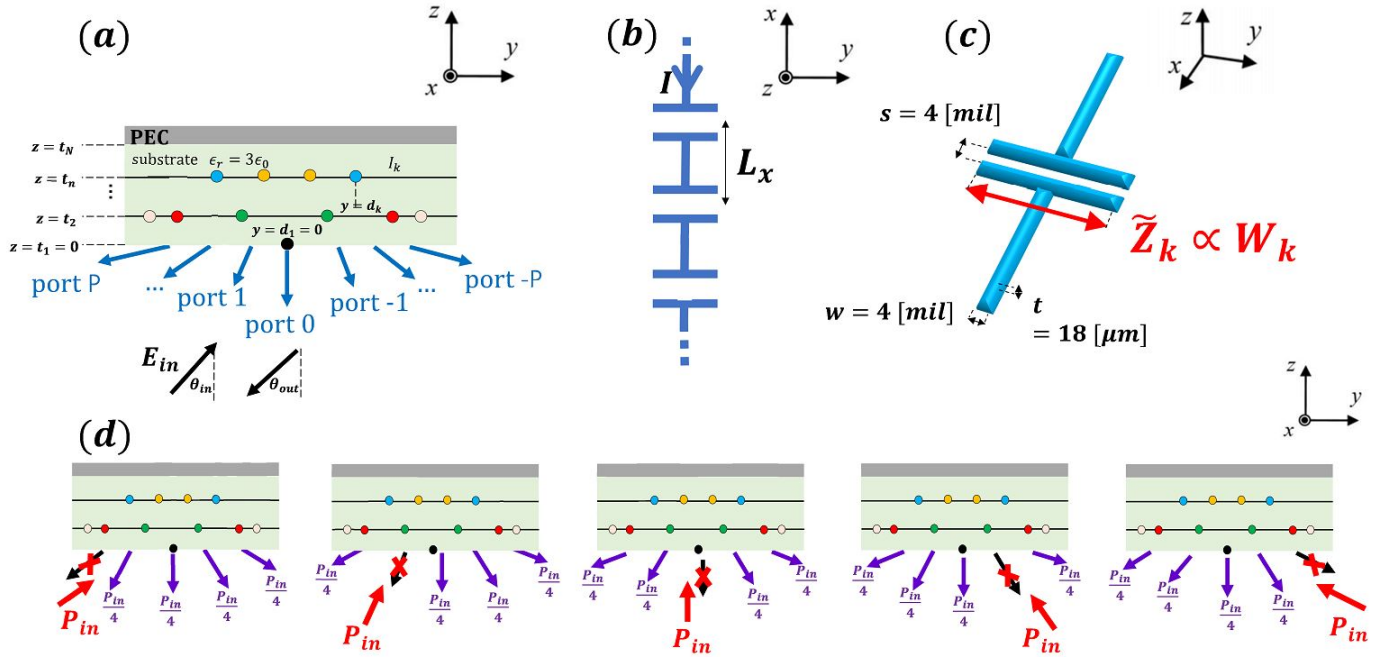


Fig. 1. (a) Physical configuration of a symmetric $M = (2P + 1)$ -port PEC-backed PCB MG diffuser. Front view of the MG, featuring K loaded copper strips distributed within the medium in the planes $z = t_n$, with horizontal and vertical offsets d_k and h_k , respectively, with respect to the reference meta-atom at $d_1 = h_1 = 0$. The structure is excited from below by a plane wave, with an angle of incidence $\theta_{in} = \theta_p$ associated with one of the input ports $p = -P, \dots, P$. The denoted output ports correspond to the propagating Floquet-Bloch modes scattered from the MG towards the angles θ_q (see also Section II-B). (b) Loaded wire meta-atom (top view). The loads repeat periodically with separation distance $L_x = \lambda/10 \ll \lambda$ along the x axis, effectively forming a distributed per-unit-length impedance \tilde{Z}_k . (c) Load detailed geometry. The width W_k of the copper printed capacitor controls the effective distributed impedance \tilde{Z}_k . (d) Multi-angle diffusive RCS reduction functionality illustration for a 5-port multichannel MG [corresponding to panel (a) with $P = 2$]. For each excitation scenario, the retrorreflection vanishes and the incident power is split equally between the remaining 4 ports.

wave impedances for each medium are given, respectively, by $k_i = \omega \sqrt{\mu_i \epsilon_i}$, $\eta_i = \sqrt{\mu_i / \epsilon_i}$, where μ_i is the permeability of the i th medium; the subscript i refers to the medium where the fields are evaluated ($i = 1, 2$). Within a period, K wires with impedances per-unit-length \tilde{Z}_k are distributed among the layers, forming the MG. To maximize the available DOFs, the wires can be vertically and horizontally offset with respect to one another, and we denote the k th wire position as $(y, z) = (d_k, h_k)$, where $d_k \in (-\Lambda/2, \Lambda/2)$, $h_k \in \{t_1, t_2, \dots, t_{N-1}\}$. The bottom metal layer is situated at the substrate-air interface, defined as the $z = t_1 = 0$ plane.

The structure is excited from below by a transverse electric (TE) polarized ($E_z = E_y = H_x = 0$) plane wave, $E_x^{inc}(y, z) = E_{in} e^{-jk_y y \sin \theta_{in} - jk_z z \cos \theta_{in}}$, with amplitude E_{in} and angle of incidence θ_{in} . According to the FB theorem, the scattered fields may couple only to a discrete set of FB modes, with a finite number of them being propagating (and the rest evanescent). Specifically, the transverse and longitudinal wavenumbers of the m th FB mode in the i th medium are determined by the period length and the incidence angle via [41]

$$k_{t,m} = k_1 \sin \theta_{in} + \frac{2\pi m}{\Lambda}, \quad \beta_{m,i} = \sqrt{k_i^2 - k_{t,m}^2} \quad (1)$$

with the square-root branch chosen such that $\Im\{\beta_{m,i}\} \leq 0$ to satisfy the radiation condition.

To find these scattered fields, we follow the formulation presented in [26], applying it to the specific case considered herein, of a metal-backed multielement MG with a single

dielectric substrate material. Correspondingly, for a given MG configuration, this is achieved by (i) evaluating the scattered fields in the absence of the MG grid (external fields); (ii) evaluating the secondary fields produced by the currents induced on the MG wires; and (iii) assessing the actual amplitudes of these induced currents and summing over all field contributions.

1) *External field contribution:* As in [26], due to the field discontinuity caused by the presence of the wires, we divide the problem domain into $N-1$ regions, where the n th region is confined between the $z = t_{n-1}$ and $z = t_n$ metalization layers. However, since the PCB MG herein features a single type of dielectric, for calculating the external field it is sufficient to treat separately only two spatial sections; specifically, we distinguish between the fields in the observation region ($n = 1$) and within the dielectric substrate ($n > 1$).

Consequently, the external field (i.e., in the absence of the MG wires) in the n th region can be written as a sum of forward and backward propagating plane waves adhering Snell's law

$$E_n^{ext}(y, z) = A_{0,n}^{ext} e^{-jk_{t_0} y - j\beta_{0,i} z} + B_{0,n}^{ext} e^{-jk_{t_0} y + j\beta_{0,i} z} \quad (2)$$

where the subscript i refers to the medium of the n th layer ($i = 1$ for $n = 1$ and $i = 2$ for $n > 1$) [cf. (1)]. The amplitudes $A_{0,n}^{ext}$ and $B_{0,n}^{ext}$ are calculated by imposing the relevant boundary conditions, namely, continuity of the tangential fields at the air-dielectric interface ($z = 0$) and vanishing of the tangential

electric field at the PEC interface ($z = t_N$), leading to

$$\begin{aligned} A_{0,1}^{\text{ext}} &= E_{\text{in}} & B_{0,1}^{\text{ext}} &= E_{\text{in}} \frac{\Gamma_0 + e^{-2j\beta_0,2t_N}}{1 + \Gamma_0 e^{-2j\beta_0,2t_N}} \\ A_{0,n>1}^{\text{ext}} &= E_{\text{in}} \frac{1 + \Gamma_0}{1 - \Gamma_0 e^{-2j\beta_0,2t_N}} & B_{0,n>1}^{\text{ext}} &= A_{0,n>1}^{\text{ext}} e^{-2j\beta_0,2t_N} \end{aligned} \quad (3)$$

where the local reflection coefficient is defined as $\Gamma_m = \frac{Z_{m,2} - Z_{m,1}}{Z_{m,2} + Z_{m,1}}$, with the TE wave impedance of the m th mode in the i th medium being $Z_{m,i} = \frac{k_i \eta_i}{\beta_{m,i}}$.

2) *Grid-induced field contribution:* Once excited by the incident field, currents would be induced on the MG wires, giving rise to secondary fields. To evaluate these grid-originated fields, we superimpose the contributions of the various wires in the MG, acting as a Λ -periodic array of electric line sources. Specifically, the electric field in the n th layer due to the (yet to be evaluated) currents I_k developing on the k th wire in each period can be written as an infinite series of FB modes

$$E_n^{(k)}(y, z) = \sum_{m=-\infty}^{\infty} E_{m,n}^{(k)}(y, z) \quad (4)$$

where the field corresponding to the m th mode can, once more, be expressed as a sum of forward and backward propagating plane waves

$$E_{m,n}^{(k)}(y, z) = A_{m,n}^{(k)} e^{-jk_t m y - j\beta_{m,i} z} + B_{m,n}^{(k)} e^{-jk_t m y + j\beta_{m,i} z}. \quad (5)$$

To find the amplitudes $A_{m,n}^{(k)}$ and $B_{m,n}^{(k)}$, we use the recursive formalism scheme described in [26], [44], applying the source conditions (tangential field discontinuity) due to the current-carrying wires in the configuration while considering multiple reflections within the grounded dielectric substrate; for brevity, we provide here only the final results.

Referring to the specific configuration considered herein [Fig. 1(a)], we once again distinguish between the wires positioned at the air-dielectric interface (external wires), and wires located within the substrate (internal wires). For the external wires, we evaluate separately the coefficients in two regions: above the wire ($1 < n < N$), and below it ($n = 1$)

$$\begin{aligned} A_{m,1}^{(k)} &= 0 & B_{m,1}^{(k)} &= -\frac{Z_{m,1} I_k}{2\Lambda} \frac{\Gamma_m + e^{-2j\beta_{m,2} t_N}}{1 + \Gamma_m e^{-2j\beta_{m,2} t_N}} \\ A_{m,n>1}^{(k)} &= \frac{Z_{m,1} I_k}{2\Lambda} \frac{-(1 + \Gamma_m)}{1 - \Gamma_m e^{-2j\beta_{m,2} t_N}} & B_{m,n>1}^{(k)} &= A_{m,n>1}^{(k)} e^{-2j\beta_{m,2} t_N}. \end{aligned} \quad (6)$$

For the internal wires located at some $z = t_{n_k}$, three regions are taken into account separately: above the wire ($n_k < n < N$), below the wire within the substrate ($1 < n \leq n_k$), and below the MG ($n = 1$)

$$\begin{aligned} A_{m,1}^{(k)} &= 0 \\ A_{m,1 < n \leq n_k}^{(k)} &= -B_{m,1 < n \leq n_k}^{(k)} \Gamma_m \\ A_{m,n > n_k}^{(k)} &= \frac{-Z_{m,2} I_k}{2\Lambda} \frac{e^{j\beta_{m,2} t_{n_k}} - \Gamma_m e^{-j\beta_{m,2} t_{n_k}}}{1 + \Gamma_m e^{-2j\beta_{m,2} t_N}}; \end{aligned} \quad (7)$$

$$\begin{aligned} B_{m,1}^{(k)} &= B_{m,1 < n \leq n_k}^{(k)} (1 - \Gamma_m) \\ B_{m,1 < n \leq n_k}^{(k)} &= \frac{-Z_{m,2} I_k}{2\Lambda} \frac{e^{j\beta_{m,2} t_{n_k}} + e^{-2j\beta_{m,2} t_N}}{1 - \Gamma_m e^{-2j\beta_{m,2} t_N}} \\ B_{m,n > n_k}^{(k)} &= A_{m,n > n_k}^{(k)} e^{-2j\beta_{m,2} t_N}. \end{aligned}$$

Subsequently, for a given MG configuration and given induced currents I_k , the total field in the n th layer can be deduced by summing the external field (2) with the MG contribution (4), reading

$$E_n^{\text{tot}}(y, z) = E_n^{\text{ext}}(y, z) + \sum_{k=1}^K \sum_{m=-\infty}^{\infty} E_{m,n}^{(k)}(y, z). \quad (8)$$

3) *Evaluation of induced currents:* To enable actual evaluation of (8), we need to assess the currents I_k induced on the loaded wires in the given configuration when illuminated by E_n^{ext} . To this end, we utilize Ohm's law, relating the total field applied on a wire to the current flowing through it via the distributed load impedance \tilde{Z}_k [Fig. 1(c)]. Explicitly, for the k th wire, this yields [41]

$$\begin{aligned} I_k \tilde{Z}_k &= E_{n_k}^{\text{ext}}(d_k, h_k) + \sum_{q \neq k} \sum_{m=-\infty}^{\infty} E_{m,n}^{(k)}(y, z) \\ &+ \sum_{m=-\infty}^{\infty} E_{m,n_k}^{(k)}(y \rightarrow d_k, z \rightarrow h_k), \end{aligned} \quad (9)$$

where the first term of the RHS represents the excitation field in the absence of the MG, the second term corresponds to the fields produced by all wires other than the wire itself at its position, and the last term corresponds to the fields produced by the wire itself, forming together the total field acting on the k th wire.

The first and second terms are calculated directly by substituting the reference wire position into (2)-(7). For the third term, due to the singularity of the Hankel function at the origin, it is not possible to use the pre-calculated terms for the grid induced fields (4)-(7). Instead, we follow the technique presented in [24], [26], and write the k th wire self-induced field as a summation of the field generated by the reference wire on its shell (using the flat wire approximation [41]), and the field produced by the other strips at the position of the reference wire (interpreted as a series of image sources), yielding

$$\begin{aligned} E_{\text{self}}^{(k)} &= \\ &- \frac{I_k}{2} \left\{ \frac{\eta_i}{\Lambda \cos \theta_{\text{in}}} + \frac{k_i \eta_i j}{\pi} \left[\log \frac{2\Lambda}{\pi w} + \frac{1}{2} \sum_{\substack{m=-\infty \\ m \neq 0}}^{\infty} \left(\frac{2\pi}{j\Lambda\beta_{m,i}} - \frac{1}{|m|} \right) \right] \right\} \\ &+ \sum_{m=-\infty}^{\infty} \left\{ \frac{k_i \eta_i}{2\Lambda\beta_{m,i}} I_k + A_{m,n_k}^{(k)} e^{-j\beta_{m,i} h_k} + B_{m,i}^{(k)} e^{j\beta_{m,i} h_k} \right\}, \end{aligned} \quad (10)$$

w being the copper trace width [Fig. 1(c)].

Since the forward and backward grid-induced field amplitudes of (5) are linearly proportional to the currents, (9) can be rewritten as

$$I_k \tilde{Z}_k = E_{n_k}^{\text{ext}}(d_k, h_k) + \sum_{q \neq k} \zeta_q^{(k)} I_q + \zeta_{\text{self}}^{(k)} I_k \quad (11)$$

where the coefficients $\zeta_q^{(k)}$ and $\zeta_{\text{self}}^{(k)}$ can be directly extracted from (5)-(7) and (10), respectively. Thus, the currents can be calculated by a simple matrix inversion

$\mathbf{I}_{\mathbf{K} \times 1} = \mathbf{\Psi}_{\mathbf{K} \times \mathbf{K}}^{-1} \mathbf{E}_{\mathbf{K} \times 1}^{\text{ext}}$, where $\mathbf{I}_{\mathbf{K} \times 1}$ is a vector composed of the induced currents I_k ; $\mathbf{E}_{\mathbf{K} \times 1}^{\text{ext}}$ is the excitation vector, containing the external field values in the wire positions $E_{n_k}^{\text{ext}}(d_k, h_k)$; and the matrix $\mathbf{\Psi}_{\mathbf{K} \times \mathbf{K}}$ is defined by

$$\mathbf{\Psi} = \begin{pmatrix} \tilde{Z}_1 - \zeta_{\text{self}}^{(1)} & -\zeta_2^{(1)} & \cdots & -\zeta_K^{(1)} \\ -\zeta_1^{(2)} & \tilde{Z}_2 - \zeta_{\text{self}}^{(2)} & \cdots & -\zeta_K^{(2)} \\ \vdots & \cdots & \ddots & \vdots \\ -\zeta_1^{(K)} & \cdots & -\zeta_{K-1}^{(K)} & \tilde{Z}_K - \zeta_{\text{self}}^{(K)} \end{pmatrix} \quad (12)$$

4) *Evaluation of load impedances:* We should recall at this stage that the MG loaded-wire meta-atoms are physically realized using copper traces in a conventional PCB configuration, featuring printed capacitors as loads [Fig. 1(a)-(c)]. Thus, to enable assessment of $\mathbf{\Psi}$ of (12), evaluate the various currents I_k , and subsequently solve the MG scattering problem, it is required to relate the effective distributed impedance \tilde{Z}_k of the various loads to the respective printed capacitor widths W_k used in practice. Following semianalytical formulas developed in previous work, we approximate the reactive part of \tilde{Z}_k as $\Im\{\tilde{Z}_k\} = -2.85 K_{\text{corr}} / (\omega L_x W_k \varepsilon_{\text{eff},r})$ [45], where W_k is the capacitor width [Fig. 1(c)], L_x is the periodicity along the x -axis [Fig. 1(b)], and K_{corr} is a frequency-dependent correction factor (estimated as $K_{\text{corr}} = 0.947[\text{mil}/\text{fF}]$ for $w = s = 4$ mil at the working frequency of $f = 20$ GHz used herein [26]). The effective relative permittivity for the external wires is given by $\varepsilon_{\text{eff},r} = \frac{\varepsilon_1 + \varepsilon_2}{2\varepsilon_0}$ for meta-atoms at the dielectric-air interface ($n = 1$), and $\varepsilon_{\text{eff},r} = \varepsilon_2/\varepsilon_0$ for the internal wires ($n > 1$), where ε_0 is the vacuum permittivity. The resistive part of the distributed impedances, related to the conductor (copper) losses, was estimated using skin depth and cross section considerations as $\Re\{\tilde{Z}_k\} \approx 14.5 \times 10^{-3}[\eta/\lambda]$ for the same operating conditions [23].

This completes the *forward* problem analysis: for given incident plane wave and MG parameters (i.e., the wire positions $(y, z) = (d_k, h_k)$ and the capacitors widths W_k), one may follow the above formalism to deduce the distributed impedances from the capacitor widths, evaluate the currents from (12) with (2), (3), (5)-(7), (10), and (11), and calculate the fields scattered off the multilayer MG towards the observer via (8) with $n = 1$.

B. Multichannel diffusive MG (synthesis)

Once the analytical model relating a given MG configuration to the fields scattered off it when illuminated from a given θ_{in} is established as in Section II-A above, we may proceed to tackle the synthesis problem at hand, defining suitable constraints on the coupling coefficients to the various reflected FB modes (for multiple excitations simultaneously in our multichannel scenario), as to facilitate the desired functionality.

As mentioned in Section I, we wish to exploit symmetry properties of the problem to reduce the overall number of constraints (leading to simpler designs with fewer DOFs). To obtain a symmetric multichannel network (about $\theta = 0^\circ$), we choose the $2P + 1$ angles of incidence spanning the effective acceptance angle range to be $\theta_{\text{in}} \in$

$\Theta \triangleq \{\arcsin(p\lambda/\Lambda) \mid p = -P, \dots, P\}$ [Fig. 1(a),(d)]. The advantage of such a choice, beyond manifesting the symmetry of the scattering scenario, is that for each of these incidence angles, the propagating scattered FB modes will be reflected to angles of the same set $\theta_{\text{out}} \in \Theta$. This would form a symmetric $M = (2P+1)$ -port network [38], where the number of channels (propagating modes) is set by Λ via $P = \lfloor \Lambda/\lambda \rfloor$ [26], promoting a broad-angle response.

Following this idea, and along the lines of [26], we can calculate the amplitude of the field $E_{q,p}$ scattered towards the q th port when the MG is excited from the p th port using (8) with $n = 1$, reading

$$E_{q,p} = B_{-p,p;1}^{\text{ext}} \delta_{q,-p} + \sum_{k=1}^K B_{q,p;1}^{(k)}. \quad (13)$$

where $B_{q,p;1}^{(k)}$ is the downwards propagating wave amplitude $B_{m,n}^{(k)}$ of (5) in Section II-A, evaluated in the observation region $n = 1$ for a scenario in which $\theta_{\text{in}} = \theta_p$, and the FB mode order⁴ m corresponds to the output angle defined by $\theta_q = -\arcsin(k_{t,m}/k_1)$; $B_{-p,p;1}^{\text{ext}}$ is the amplitude of the reflected external field $B_{0,1}^{\text{ext}}$ of (2) for the same excitation scenario $\theta_{\text{in}} = \theta_p$, which only contributes in case that the q th port corresponds to the specular reflection, namely, $q = -p$.

With these definitions, we describe the multichannel MG system using a $M \times M$ scattering matrix (S-matrix), where the input and output ports correspond to the FB modes associated with the excitation angles $\theta_p \in \Theta$ and the scattering angles $\theta_q \in \Theta$, respectively. Specifically, the fraction of power coupled to the q th port by the MG when excited from the p th port can be evaluated via the corresponding scattering coefficient $S_{q,p}$ using (13), reading [24]

$$|S_{q,p}|^2 = \left| \frac{E_{q,p}}{E_{\text{in}}} \right|^2 \frac{\cos \theta_q}{\cos \theta_p} \quad (14)$$

This scattering matrix representation allows us to conveniently stipulate the constraints guaranteeing the desired MG functionality, namely, multi-angle monostatic and bistatic RCS reduction. To achieve these goals simultaneously, we demand that for each excitation scenario, coupling to the retroreflection channel would vanish ($S_{p,p} = 0$), and the incident power would be uniformly scattered into the other available channels ($|S_{q,p}|^2 = 1/(M-1)$, $\forall p \neq q$). The matrix describing the *power* scattered from each port at a given excitation scenario can thus be written explicitly as⁵

⁴In contrast to [26], we use port indices q and p for the scattering field amplitudes, the interpretation of which in terms of incidence/reflection angles is fixed for all excitation scenarios considered herein, rather than using directly the FB mode orders m , whose associated scattering angles vary with the angle of incidence. For instance, the specular reflection would always be associated with the fundamental $m = 0$ FB mode, while in practice it could refer to different ports (different reflection angles) for different excitations. Naturally, to address systematically the multichannel device presented herein, we found the former notation scheme to be more suitable.

⁵As known, a 3-port matched network could not be realized by a passive and lossless configuration [46] such as the one prescribed in (15); therefore, we restrict the number of channels considered herein to $M > 3$.

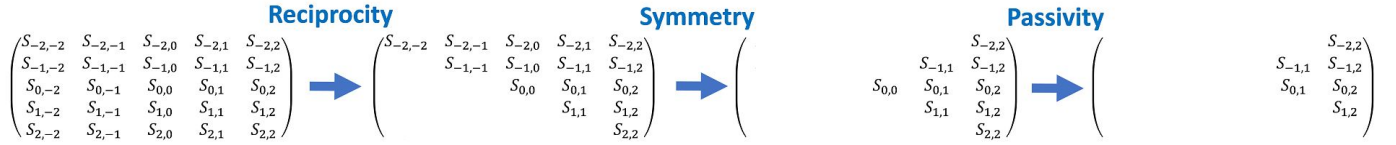


Fig. 2. Identification of the independent scattering parameters in a 5×5 ($P = 2, M = 5$) S-matrix, harnessing reciprocity, symmetry, and passivity properties of the configuration to yield a compacted set of constraints (see Section II-B).

$$|\mathbf{S}|^2 = \begin{pmatrix} 0 & \frac{1}{M-1} & \cdots & \frac{1}{M-1} \\ \frac{1}{M-1} & 0 & \cdots & \frac{1}{M-1} \\ \vdots & \cdots & \ddots & \vdots \\ \frac{1}{M-1} & \frac{1}{M-1} & \cdots & 0 \end{pmatrix} \quad (15)$$

It is important to note that in the synthesis scheme we develop here the constraints are applied *directly* to the nonlinear relations tying the scattering parameters to the MG configuration (14). This is in contrast to the method laid out in [26], where the desired coupling coefficients of the propagating FB modes were first substituted into (8) [or (13)] to form a linear set of equations, treating the induced currents as the only unknowns. Following this approach of [26], for given meta-atom distribution, the induced currents (and subsequently the load impedances) are determined in a unique manner through this linear system, an observation that was integrated into the design procedure. Correspondingly, the synthesis method adopted therein merely required from the MATLAB solver `lsqnonlin` to find these meta-atom coordinates that would lead to a passive and lossless design under this set of linear equations. However, an implicit requirement for the utilization of such a scheme is that the number of unknowns (induced currents) in the linear system would be equal to or larger than the number of equations (propagating FB modes), i.e. $K \geq M$, which puts a lower bound on the number of meta-atoms per period required for *each* considered functionality (design goal) [26].

Herein, we relax this bound by allowing more flexibility to the inverse problem solver, looking simultaneously for suitable meta-atom locations *as well as* suitable passive loads to meet the multiple (multichannel) constraints, without explicitly invoking the linear relations between the currents and the FB modal amplitudes for fixed meta-atom placements. Since in such a general nonlinear solution scheme the meta-atom coordinates serve as legitimate DOFs which can be used independently from the induced currents, this results in great benefits in terms of scatterer density (reduced number of meta-atoms per period), especially for multifunctional MGs. An additional benefit of this approach is that it does not require stipulation of the complex FB modal *field* amplitudes; instead, the constraints can be defined in terms of the desired fraction of incident *power* coupled to each mode (channel), which is a far less strict limitation, and may be satisfied with fewer DOFs (simpler designs).

In fact, we can decrease the number of required DOFs even further if we harness the S-matrix properties, which should be inherently satisfied by the MG as we design it, reducing

the number of independent constraints in our problem. Specifically, we recall that the MG is composed of reciprocal, passive and (ideally) lossless elements (highly-conducting strips and low-loss dielectrics), and that the ultimate configuration should be symmetric about the \widehat{xz} plane. Reciprocity implies that imposing constraints over $S_{p,q}$ immediately determines $S_{q,p}$, removing the need to explicitly consider the latter (Fig. 2). Furthermore, the symmetric nature of the MG requires that $S_{p,q} = S_{-p,-q}$ [Fig. 1(a),(d)], making it sufficient to apply constraints only on one of these S-parameters. Lastly, power conservation implies that the S-matrix should be unitary, and, in particular, the absolute square of the S-parameters in each row or column should sum up to unity [46]. In other words, once all the S-parameters but one in a row q' are determined, the power coupled to this last element p' is bound by $1 - \sum_{p \neq p'} |S_{q',p}|^2$, and thus need not be constrained by our synthesis procedure⁶ (Fig. 2). In summary, as illustrated in Fig. 2, for a $M = 2P + 1$ port network, the number of independent elements is reduced by reciprocity, symmetry, and passivity from the initial $M \times M = (2P + 1)^2$ to $(P + 1)^2 - (P + 1) = P(P + 1)$, corresponding to a dramatic reduction in the required constraints.

With the number of independent constraints established, we may proceed to executing the synthesis procedure based on a suitable number of DOFs (elements per period and their coordinates). To this end, we use the forward problem analytical formulation of Section II-A and solve the inverse problem defined by the constraints (15) using the MATLAB library function `lsqnonlin`. Since the problem is nonlinear, different initial values of (d_k, h_k, W_k) provided to the function result in convergence to different solutions. To search for an optimal configuration, we run the function with different random initial values 50 times (overall runtime < 1 min on a standard desktop computer), and choose out of the resulting 50 sets of MG designs the one with the smallest residual (the square norm of the deviation from the desired S-matrix, as defined in (15)). Since this process provides numerous options for detailed fabrication-ready PCB layouts, we may choose a configuration which will best match practical fabrication constraints (low profile, layer thicknesses that match commercially available dielectric laminates, etc.) and proceed towards implementation.

⁶Since our aim is to reduce the RCS in each observation angle, enforcing an upper bound on the scattering is sufficient.

III. RESULTS AND DISCUSSION

A. Prototype

To verify the developed synthesis method, we follow the scheme described in Section II to design a multichannel MG diffuser for multi-angle monostatic and bistatic RCS reduction. In particular, we aim at realizing a 5-channel MG ($M = 5$) at $f = 20$ GHz ($\lambda \approx 15$ mm), corresponding to an S-matrix (15) which manifests zero retroreflection, and equally divides the incident power among the four remaining channels ($|S_{q,p}|^2 = 0.25, \forall p \neq q$). Since we wish the chosen scattered wave (FB mode) trajectories to span well the reflection angular range $\theta \in (-90^\circ, 90^\circ)$, we set the periodicity to $\Lambda = \lambda / \sin(29^\circ) \approx 31$ mm, leading to a set of five propagating FB modes, defining the input and output channel propagation angles as $\theta_0 = 0^\circ$, $\theta_{\pm 1} = \pm \arcsin(\lambda/\Lambda) = \pm 29^\circ$, and $\theta_{\pm 2} = \pm \arcsin(2\lambda/\Lambda) = \pm 75.84^\circ$ (Section II-B).

We attempt to design the desired MG prototype based on a configuration composed of two metallization layers ($N = 3$) of 0.5oz copper traces (copper thickness $t = 18\mu\text{m}$), embedded within a Rogers RO3003 ($\epsilon_{\text{sub}} = 3\epsilon_0, \tan \delta = 0.001$) substrate, comprising three meta-atoms per period ($K = 3$). The first meta-atom (loaded wire) is positioned in the origin at the air-dielectric interface (d_1, h_1) = (0, 0), while the second and third meta-atoms are located at (d_2, h_2) and (d_3, h_3) within the substrate. As discussed in Section II-B above, to reduce the number of independent constraints and subsequently the required number of DOFs, we impose a symmetric configuration, namely, the internal wires are designed with identical capacitor widths $W_2 = W_3$ (identical loads), and are positioned symmetrically about the origin ($d_2 = -d_3, h_2 = h_3$), as depicted in Fig. 3.

Applying the constraints (15) via the methodology described in Section II yields a suitable MG design, featuring meta-atoms at (d_1, h_1) = (0, 0) and (d_3, h_3) = ($-d_2, h_2$) = (0.3507 λ , 0.1187 λ) = (5.3mm, 1.8mm) below the metallic mirror at $z = t_3 = 0.1935\lambda = 2.9$ mm, with printed capacitors of widths $W_1 = 1.56$ mm and $W_2 = W_3 = 1.18$ mm. Once the geometric parameters are thus set, we may readily evaluate the S-matrix of the MG by solving the forward problem (8)-(14) with the finalized (d_k, h_k, W_k), yielding

$$|\mathbf{S}|^2 = \begin{pmatrix} 0.02 & 0.24 & 0.23 & 0.25 & 0.23 \\ 0.24 & 0.01 & 0.24 & 0.25 & 0.25 \\ 0.23 & 0.24 & 0.04 & 0.24 & 0.23 \\ 0.25 & 0.25 & 0.24 & 0.01 & 0.24 \\ 0.23 & 0.25 & 0.23 & 0.24 & 0.02 \end{pmatrix} \quad (16)$$

We note that the matrix agrees well with the desired scattering goal (15) for our case ($M = 5$). As expected, the matrix corresponds to a reciprocal, symmetric, and passive system.

To verify the theoretical predictions, a single period of the prototype MG was modeled in CST Microwave Studio and simulated under periodic boundary conditions. Since in practice, the desired layer configuration in the fabricated device was realized by cascading laminates of standard thicknesses bonded using 2 mil-thick Rogers 2929 bondply ($\epsilon_{\text{sub}} = 2.94\epsilon_0$

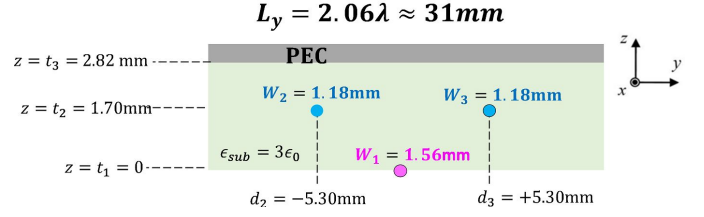


Fig. 3. Physical configuration of the symmetric 5-channel MG prototype synthesized in Section III, designed to provide multi-angle monostatic and bistatic RCS reduction at $f = 20$ GHz (side view, only a single period is shown).

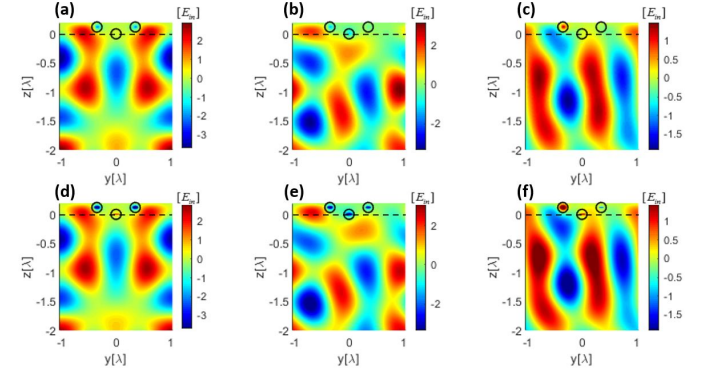


Fig. 4. Total electric field distributions $\Re\{E_x(y, z)\}$ for the prototype MG of Fig. 3 when illuminated by a plane-wave from (a),(d) $\theta_{\text{in}} = 0^\circ$, (b),(e) $\theta_{\text{in}} = 29^\circ$, and (c),(f) $\theta_{\text{in}} = 75.84^\circ$, as predicted by the analytical model [(a)-(c)] and as recorded in full-wave simulation [(d)-(f)]. Meta-atoms are denoted by black circles; substrate/air interface is marked by a dashed line.

and $\tan \delta = 0.003$), we defined this actual structure in the full-wave solver for the final verification purposes. Ultimately, also due to limited availability in real time, the manufactured MG featured total thickness of $t_3 = 111$ mil = 2.82 mm, with the meta-atoms positioned at $h_1 = 0, h_2 = h_3 = 67$ mil = 1.70 mm, slightly away from the designated planes. The simulated S-matrix of the corresponding (actual) MG was found to be

$$|\mathbf{S}|^2 = \begin{pmatrix} 0.02 & 0.26 & 0.22 & 0.21 & 0.27 \\ 0.26 & 0.00 & 0.21 & 0.28 & 0.24 \\ 0.22 & 0.24 & 0.06 & 0.24 & 0.22 \\ 0.24 & 0.28 & 0.21 & 0.00 & 0.26 \\ 0.27 & 0.21 & 0.22 & 0.26 & 0.02 \end{pmatrix} \quad (17)$$

The simulated S-mat shows overall good agreement with the analytically predicted one (16); the observed minor deviations can be attributed to the slight discrepancies between the actual fabricated model and the theoretical design discussed in the previous paragraph. Furthermore, Fig. 4 compares the analytically predicted scattered fields to the full-wave simulated ones for the three designated angles of incidence, namely, $\theta_{\text{in}} = 0^\circ$ [(a),(d)], $\theta_{\text{in}} = 29^\circ$ [(b), (e)], and $\theta_{\text{in}} = 75.84^\circ$ [(c),(f)], revealing excellent agreement. These results further establish the reliability of the analytical model, demonstrating its usefulness for the design of realistic multichannel PCB MGs.

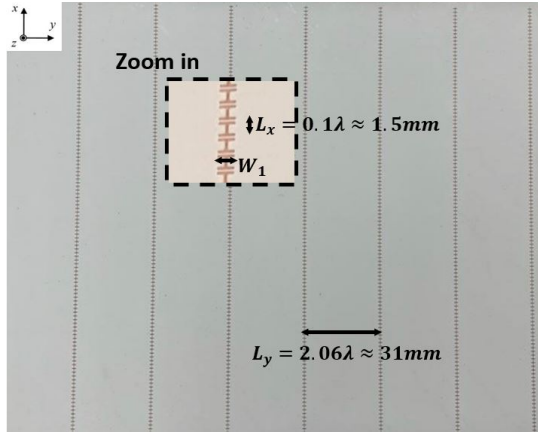


Fig. 5. The fabricated MG prototype, corresponding to Fig. 3 (top view). Only the $z=0$ layer (containing the $k = 1$ wire) is visible. Inset: a close-up view of six capacitive loads on one of the meta-atoms.

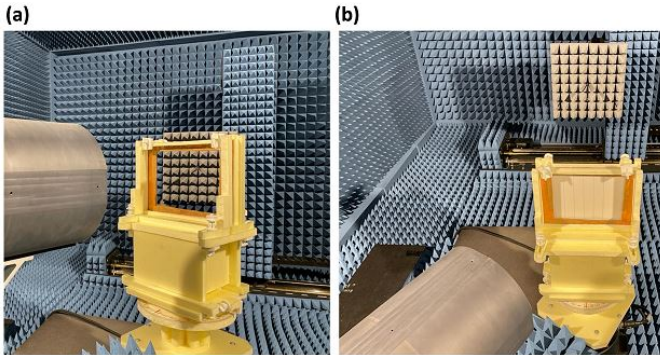


Fig. 6. Experimental setup used for characterization of the multichannel MG prototype. (a) Reference measurement using a metallic frame, enabling proper evaluation of the effective excitation power interacting with the MG active area (no DUT). (b) Characterization of the MG under test in the cylindrical near-field measurement system, conducted under illumination by the Gaussian beam antenna, tilted to form a prescribed angle of incidence θ_{in} .

B. Experiment

After this validation of the theoretical model, and without any further optimization, we used the corresponding PCB layout (Fig. 3) to fabricate a $9'' \times 12''$ board (*PCB Technologies Ltd.*, Migdal Ha'Emek, Israel); the manufactured prototype is presented in Fig. 5. The MG device under test (DUT) was characterized in an anechoic chamber at the Technion using a near-field measurement system (*MVG/Orbit-FR Engineering Ltd.*, Emek Hefer, Israel). In the chamber, the MG was positioned on a foam holder in front of a Gaussian beam antenna (Millitech, Inc., GOA-42-S000094, focal distance of $196\text{mm} \approx 13\lambda$), illuminating the device with a quasi-planar wavefront (Fig. 6). Due to blockage effects presented by the Gaussian beam antenna when scanning at wide angles, we have placed the MG at a larger distance from the Gaussian beam antenna, corresponding to $430\text{mm} \approx 29\lambda$. Nonetheless, as can be deduced from previous work [47], the focal region is large enough to provide a sufficiently collimated beam even at this distance, enabling proper characterization of the DUT.

To facilitate the manufacturing process, the MG circumference was partly sacrificed to accommodate metallic markings

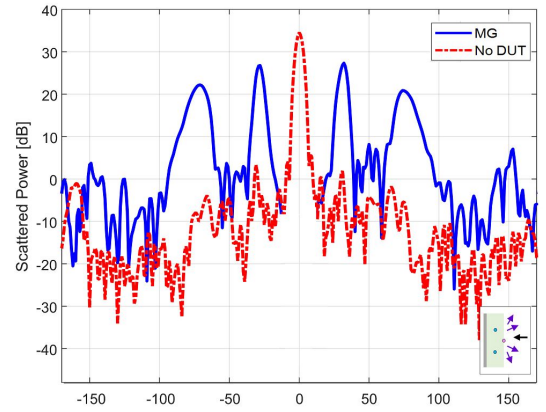


Fig. 7. Experimentally recorded scattering pattern for normal excitation [input port $p = 0$ in Fig. 1(a)] at the operating frequency of $f = 20$ GHz. The measurements are conducted once in the absence of the MG [dash-dotted red, cf. Fig. 6(a)] and in the presence of the MG [solid blue, cf. Fig. 6(b)], with the former serving as a reference for the input power.

and drilled holes used for accurate alignment during fabrication, leaving an active area smaller than the overall $9'' \times 12''$ board size. Therefore, to properly calibrate our measurements and avoid interaction with these irrelevant scatterers, we attached to the foam holder a metallic frame covering these markings, allowing quantification of the effective reference excitation power which illuminates the MG area in reality [Fig. 6(a)].

C. Characterization

By rotating the foam holder about its axis, the alignment between the Gaussian beam antenna and the MG was tuned such that the DUT scattering properties for different angles of incidence could be probed. In particular, measurements were performed for the excitation angles corresponding to the designated input ports of the multichannel MG [Fig. 6(b)]. For each of these angles of incidence, a cylindrical near-field measurement was performed, recording the scattering pattern across the frequency range $f \in [18, 22]$ GHz. The measurement was conducted by rotating together the Gaussian beam antenna and the MG (aligned to a certain illumination angle θ_{in}) around a near-field probe situated at a distance of $850\text{mm} \approx 57\lambda$ away from the MG, collecting the scattered fields. The far field patterns were then deduced by the system's postprocessing software from the near field measurements using the equivalence principle [48].

Figure 7 shows such representative scattering patterns, recorded for normal incidence [input port $p = 0$ in Fig. 1(a)] at the operating frequency of $f = 20$ GHz. As seen, in the absence of the DUT (dashed red curve), a high-gain beam peaking at $\theta = 0^\circ$ is recorded in transmission, quantifying the input power effectively interacting with the MG. Once the MG is placed in the holder (solid blue), the expected diffusive scattering is observed, with $M - 1 = 4$ dominant beams. Although these beams peak around the designated output port angles $\theta_{\pm 1} \approx \pm 29^\circ, \theta_{\pm 2} \approx \pm 75.84^\circ$, a closer examination reveals that the exact maxima occur at $\theta_1 = 31^\circ, \theta_{-1} = -28^\circ, \theta_2 = 73^\circ$, and $\theta_{-2} = -71^\circ$. These results lead to two observations. First, the asymmetry in the recorded peak

angles implies that the limited (manual) alignment accuracy of the system may introduce angular deviations of up to around 1° in measurements. Second, for large deflection angles $\theta_{\pm 2}$, the main lobe maxima shift towards lower angular values, which is attributed to the reduced effective aperture size at these near-grazing angles [49].

Another aspect that is highlighted by Fig. 7 is the inability of the described (*bistatic*) measurement setup to measure the scattered power for $\theta_{\text{in}} = \theta_{\text{out}}$ (manifested in the absence of measured data points around $\theta = 0$ in the plot when the MG is present). Since in our near-field system the probe and Gaussian beam antenna cannot be aligned to the same angle (otherwise they will physically collide), an alternative method (*monostatic*) should be used to evaluate retroreflection. Specifically, we connect to this end the Gaussian beam antenna to a dedicated vector network analyzer (4-port Keysight E5080B ENA), functioning as both the transmitter and the receiver for this measurement. Subsequently, the recorded reflection coefficient (S_{11}) provides a measure for the amount of retroreflected power. To quantify the fraction of power coupled to this channel, we compare this value with a reference measurement conducted with a planar metal plate matching the dimensions of the MG.

Finally, for both bistatic and monostatic setups, we evaluate the power coupled to each channel by considering the ratio between the peak measured gain values of the MG scattering patterns $G_{\text{MG}}(\theta_{\text{out}})$ and the reference measurement $G_{\text{ref}}(\theta_{\text{in}})$ quantifying the effective incident power, taking in account the differences in the effective aperture size [22], [26], [47], [50]

$$\eta_{\text{tot}} = \frac{G_{\text{MG}}(\theta_{\text{out}})}{G_{\text{ref}}(\theta_{\text{in}})} \frac{\cos \theta_{\text{in}}}{\cos \theta_{\text{out}}}, \quad (18)$$

which for the retroreflection case $\theta_{\text{in}} = \theta_{\text{out}}$ simply reduces to the ratio of the measured reflection coefficients in the input of the Gaussian beam antenna.

Figure 8 presents the measured frequency dependency of the power coupled to each propagating mode (output channels), for illumination from the predefined excitation angles (input channels⁷), compared to the simulation results. The graphs indicate good correspondence between the simulated and experimentally recorded scattering patterns in the measured frequency range. The minor differences observed [mainly in panels (a)-(d)] between theoretical predictions and experimental estimations can be attributed to limited angular alignment accuracy in our setup (see discussion after Fig. 7), which may introduce small errors in the actual angle of incidence with respect to the desired θ_{in} ; possible fabrication inaccuracies and material parameter tolerances may also contribute to such deviations.

The measured frequency response is further affected by the periodic nature of the designed multichannel MG. Indeed, certain effects observed in Fig. 8 stem from the variation of the particular propagation angle associated with the scattering

⁷The measurement setup did not allow proper characterization of the MG when illuminated by large oblique angles of incidence, mainly due to the small effective aperture size for such angles (proportional to $\cos \theta_{\text{in}}$ [48]). Thus, Fig. 8 only considers $\theta_{\text{in}} = 0^\circ, \pm 29^\circ$, whereas the performance associated with $\theta_{\text{in}} = \pm 75.84^\circ$ is deduced from reciprocity considerations (see discussion surrounding Fig. 9 later on).

towards the p th port, as dictated by (1). Specifically, when reducing the operating frequency, higher-order FB modes are driven into the invisible region, eventually becoming evanescent (and thus cannot outcouple real power). This explains the low-frequency behaviour observed in Fig. 8(c), (d), and (f), where the scattering towards the presented port abruptly vanishes when a certain "cutoff" frequency is crossed⁸. Such a crossing has an impact on the distribution of power amongst the other FB modes as well, as can be seen, for instance, in the substantial growth in the power coupled to the $p = 0$ port around $f = 19.2$ GHz in Fig. 8(h), stemming from the cutoff identified for the same excitation scenario in Fig. 8(f). Similarly abrupt trend changes can be spotted in Fig. 8(a) and (b) around the cutoff frequencies $f = 18.8$ GHz and $f = 19.6$ GHz, associated, respectively, with the FB modes characterized in Fig. 8(c) and (d) for the same angle of incidence $\theta_{\text{in}} = 29^\circ$.

Another effect of the modal frequency dependency manifested by (1) is related to the retroreflection phenomena. While for $\theta_{\text{in}} = 0$, retroreflection coincides with the specular reflection and thus always directed towards broadside [Fig. 8(h)], for other illumination angles (e.g., $\theta_{\text{in}} = 29^\circ$) the multichannel scattering scenario would not include ports with $\theta_{\text{out}} = \theta_{\text{in}}$ for measurements outside the designated operating frequency. In other words, significant power could be recorded at $\theta_{\text{out}} = \theta_{\text{in}}$ only for a limited range of frequencies around the design working point $f = 20$ GHz (unless $\theta_{\text{in}} = 0$), whereas outside this range coupling towards this direction would not be allowed as per the FB theorem. Following this observation, we present the retroreflection data for $\theta_{\text{in}} = 29^\circ$ only for the range $f \in [19.5, 20.5]$ GHz [Fig. 8(e)], in which the deviation of θ_{out} from θ_{in} is still mild such that the retroreflection measurement is still meaningful⁹.

Overall, it can be seen that the MG performs well around the designated operating frequency, suppressing coupling to the retroreflection mode while distributing the scattered power amongst the other channels. These properties are further apparent from Fig. 9, quantifying the fraction of power coupled to the various output ports for each of the considered excitations $\theta_{\text{in}} = 0^\circ$ (left), $\theta_{\text{in}} = 29^\circ$ (center), and $\theta_{\text{in}} = 75.84^\circ$ (right) at $f = 20$ GHz. For comparison, four sets of data are presented for each scenario. The first row (Analytical) corresponds to the predictions of the analytical model as output by the synthesis procedure (8)-(14), in correspondence with (16); the second row (Full-wave: design) presents the scattered power as recorded in full-wave simulations for this chosen design; the third row (Full-wave: actual) indicates the expected effects on the MG performance when the actual

⁸In Fig. 8(c)-(d), finite power is recorded at frequencies lower than the theoretical "cutoff" frequency [calculated as $f = 18.8$ GHz for (c), and $f = 19.6$ GHz for (d)]. This may be attributed again to small alignment errors due to the manual mechanism used in the experiment (see discussion after Fig. 7), correspondingly causing minor deviations in the angle of incidence. Due to the high angular sensitivity for this extreme deflection towards near-grazing angles, even such minor deviations would be sufficient to shift the "cutoff" frequency below $f = 18$ GHz [cf. (1)].

⁹Recall that for the retroreflection measurement the Gaussian beam is static with respect to the MG, relying on the assumption that the main scattering would be towards $\theta_{\text{out}} = \theta_{\text{in}}$ (Section III).

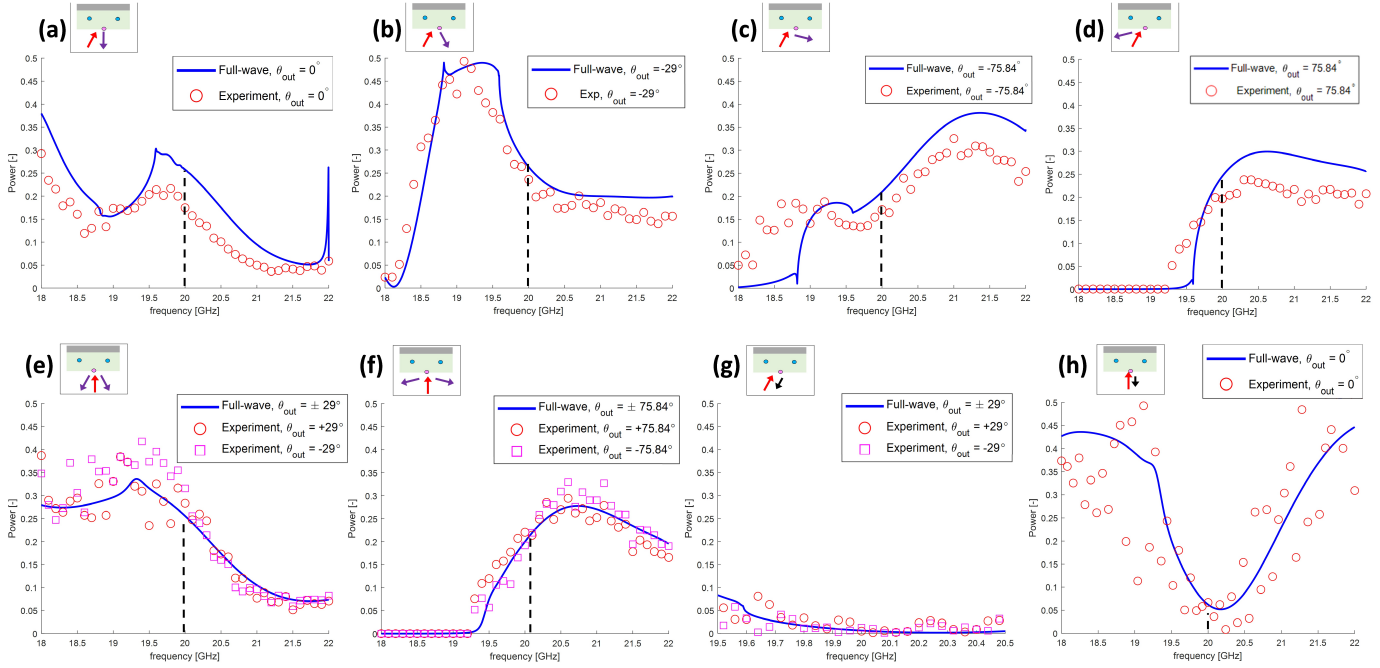


Fig. 8. Frequency response of the prototype MG diffuser of Fig. 3. The fraction of incident power coupled to each of the output ports for two different excitation scenarios $\theta_{in} = 29^\circ$ [(a)-(d),(g)] and $\theta_{in} = 0^\circ$ [(e),(f),(h)] is plotted as a function of the frequency. The experimental results (red circles and magenta squares) are compared with the results obtained via full-wave simulation (solid blue) for the input and output ports associated with the angles (a) $\theta_{in} = 29^\circ, \theta_{out} = 0^\circ$; (b) $\theta_{in} = 29^\circ, \theta_{out} = -29^\circ$; (c) $\theta_{in} = 29^\circ, \theta_{out} = -75.84^\circ$; (d) $\theta_{in} = 29^\circ, \theta_{out} = 75.84^\circ$; (e) $\theta_{in} = 0^\circ, \theta_{out} = 29^\circ$ (red circles), $\theta_{out} = -29^\circ$ (magenta squares); (f) $\theta_{in} = 0^\circ, \theta_{out} = 75.84^\circ$ (red circles), $\theta_{out} = -75.84^\circ$ (magenta squares); (g) $\theta_{in} = 29^\circ, \theta_{out} = 29^\circ$ (red circles), and $\theta_{in} = -29^\circ, \theta_{out} = -29^\circ$ (magenta squares). (h) $\theta_{in} = 0^\circ, \theta_{out} = 0^\circ$; Insets depict the characterization scenario, while dashed vertical lines mark the operating frequency $f = 20$ GHz.

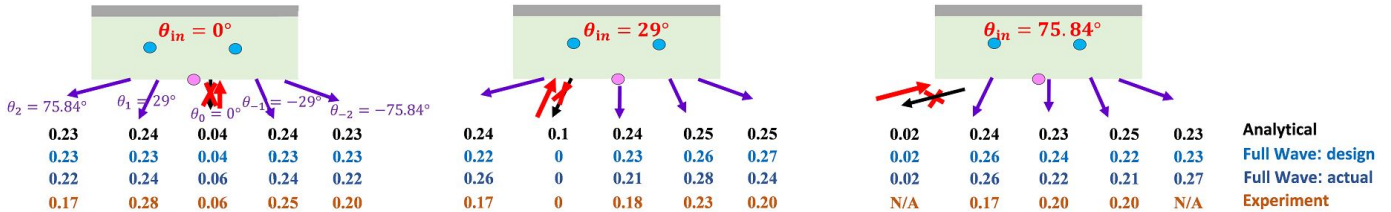


Fig. 9. Quantification of the scattering parameters of the prototype MG diffuser of Fig. 3. The fraction of incident power coupled to each of the output ports for all five considered excitation scenarios (input ports) is presented, as evaluated at the operating frequency $f = 20$ GHz [due to symmetry, only three excitation scenarios are presented, cf. (16), (17)]. The analytical predictions (black) are compared with the scattered power as recorded in full-wave simulations for the optimal design (light blue) and the one eventually realized with the available laminate stack (dark blue), as well as with the results obtained in the experiment (orange). Due to the setup limitations, results for the grazing angle excitation scenarios of $\theta_{in} = \pm 75.84^\circ$ were not recorded; where possible, these were deduced by reciprocity considerations.

laminate stack used for the fabricated prototype is considered in CST, previously reported in (17); and the fourth row (Experiment) documents the scattered power as measured in the anechoic chamber. As can be clearly seen, the collected data show good agreement between analytically computed, simulated and measured power coupling to each port. Even the constraints posed by laminate availability did not deteriorate significantly the MG operation, implying a certain robustness against fabrication errors. From a RCS reduction perspective, for all considered angles of incidence in this multichannel scenario, the measured retroreflection was found to be lower than 6% of the incident power, and the maximal power coupled to a single direction (output port) did not exceed 28%. Hence,

the presented results verify the efficacy of the proposed MG in realizing intricate multi-angle scattering management, relying on a PCB fabrication-ready sparse configuration designed using a full-wave-optimization-free methodology.

Before we conclude, we should note that although the device was designed to equally divide the power between $M - 1 = 4$ ports only when excited from one of the $M = 5$ designated angles of incidence Θ , it actually reduces the maximal scattering for other excitation angles as well. Specifically, examining the angular response by both full-wave simulations and analytically over a broader range reveals that the power coupled to a single direction (FB mode) does not exceed 45% of the incident power, for all excitation angles in

the range of $|\theta_{in}| \leq 80^\circ$ excluding a small fragment around $\theta_{in} = 25^\circ$. Clearly, increasing the periodicity Λ beyond $P\lambda$ for some $P \in \mathbb{N}$ would correspondingly increase the "sampling" resolution of the angular domain with $M = 2P + 1$ symmetric channels, while at the same time reduce the power fraction scattered to each channel $\propto 1/(M - 1)$. Naturally, this would require more DOFs (meta-atoms per periods) to meet the increased number of constraints (S parameters); on the other hand, it is expected that if the angular density of the channels is sufficiently high (the angular difference between adjacent angles θ_p would be sufficiently small), the RCS reduction performance would be maintained more evenly across the entire angular range [40].

IV. CONCLUSION

In this paper, we introduced a rigorous semianalytical method for designing PCB-compatible multichannel MG diffrusers, enabling reduction of monostatic and bistatic RCS for multiple angles of incidence simultaneously. By adopting a symmetric and passive MG construct, along with a synthesis procedure that clearly identifies the minimal required number of DOFs and effectively exploits them, a highly-sparse configuration is obtained. Specifically, the demonstrated prototype achieves multi-angle functionality spreading over a wide angular range with only three subwavelength loaded wires within a two-wavelength period, compared to the typical number of 10 – 20 polarizable particles per period that would be used in a conventional (single-functionality) MS with the same periodicity. Moreover, the presented model, verified experimentally, enables producing a complete fabrication-ready design without relying on time consuming full-wave optimization. Since the analytical scheme is general, the methodology can be used, in principle, to exercise control over an arbitrary number of diffraction modes (by including additional meta-atoms per period) and meet the requirements of versatile multifunctional scattering scenarios. In the context of the explored RCS reduction problem, this generality can be harnessed to further enhance the diffuser performance by increasing the number of channels, correspondingly improving the angular response as well as the bistatic RCS reduction. These results and conceptual observations establish a reliable foundation for the design of sparse multi-angular metagratings for a variety of electromagnetic applications.

ACKNOWLEDGMENT

This research was supported by the Israel Science Foundation (Grant No. 1540/18) as well as the PMRI – Peter Munk Research Institute - Technion. The authors also wish to thank Rogers Corporation for providing part of the laminates used in work, and the Keysight team in Israel for providing the 4-port VNA used for the retroreflection measurements.

REFERENCES

- [1] E. F. Knott, J. F. Schaeffer, and M. T. Tully, *Radar Cross Section*. SciTech Publishing, 2004.
- [2] S. B. Glybovski, S. A. Tretyakov, P. A. Belov, Y. S. Kivshar, and C. R. Simovski, "Metasurfaces: from microwaves to visible," *Phys. Rep.*, vol. 634, pp. 1–72, May 2016.
- [3] Y. Ra'di, C. Simovski, and S. Tretyakov, "Thin perfect absorbers for electromagnetic waves: theory, design, and realizations," *Phys. Rev. Appl.*, vol. 3, no. 3, p. 037001, Mar. 2015.
- [4] D. Lim and S. Lim, "Ultrawideband electromagnetic absorber using sandwiched broadband metasurfaces," *IEEE Antennas Wirel. Propag. Lett.*, vol. 18, no. 9, pp. 1887–1891, Sep. 2019.
- [5] A. Murugesan, K. T. Selvan, A. Iyer, K. V. Srivastava, and A. Alphones, "A review of metasurface-assisted RCS reduction techniques," *Prog. Electromagn. Res. B*, vol. 94, pp. 75–103, 2021.
- [6] M. Paquay, J.-C. Iriarte, I. Ederra, R. Gonzalo, and P. de Maagt, "Thin AMC structure for radar cross-section reduction," *IEEE Trans. Antennas Propag.*, vol. 55, no. 12, pp. 3630–3638, Dec. 2007.
- [7] J. C. Iriarte Galarregui, A. Tellechea Pereda, J. L. Martínez De Falcón, I. Ederra, R. Gonzalo, and P. De Maagt, "Broadband radar cross-section reduction using AMC technology," *IEEE Trans. Antennas Propag.*, vol. 61, no. 12, pp. 6136–6143, 2013.
- [8] A. Ghayekhloo, M. Afsahi, and A. A. Orouji, "An optimized checkerboard structure for cross-section reduction: producing a coating surface for bistatic radar using the equivalent electric circuit model," *IEEE Antennas Propag. Mag.*, vol. 60, no. 5, pp. 78–85, Oct. 2018.
- [9] J. Chen, Q. Cheng, J. Zhao, D. S. Dong, and T.-J. Cui, "Reduction of radar cross section based on a metasurface," *Prog. Electromagn. Res. C*, vol. 146, pp. 71–76, 2014.
- [10] T. J. Cui, M. Q. Qi, X. Wan, J. Zhao, and Q. Cheng, "Coding metamaterials, digital metamaterials and programmable metamaterials," *Light Sci. Appl.*, vol. 3, no. Oct., pp. e218–e218, Oct. 2014.
- [11] L.-H. Gao, Q. Cheng, J. Yang, S.-J. Ma, J. Zhao, S. Liu, H.-B. Chen, Q. He, W.-X. Jiang, H.-F. Ma, Q.-Y. Wen, L.-J. Liang, B.-B. Jin, W.-W. Liu, L. Zhou, J.-Q. Yao, P.-H. Wu, and T.-J. Cui, "Broadband diffusion of terahertz waves by multi-bit coding metasurfaces," *Light Sci. Appl.*, vol. 4, no. 9, pp. e324–e324, Sep. 2015.
- [12] K. Chen, Y. Feng, Z. Yang, L. Cui, J. Zhao, B. Zhu, and T. Jiang, "Geometric phase coded metasurface: from polarization dependent directive electromagnetic wave scattering to diffusion-like scattering," *Sci. Rep.*, vol. 6, no. 1, p. 35968, Dec. 2016.
- [13] M. Moccia, S. Liu, R. Y. Wu, G. Castaldi, A. Andreone, T. J. Cui, and V. Galdi, "Coding metasurfaces for diffuse scattering: scaling laws, bounds, and suboptimal design," *Adv. Opt. Mater.*, vol. 5, no. 19, p. 1700455, Oct. 2017.
- [14] M. Feng, Y. Li, Q. Zheng, J. Zhang, Y. Han, J. Wang, H. Chen, S. Sai, H. Ma, and S. Qu, "Two-dimensional coding phase gradient metasurface for RCS reduction," *J. Phys. D*, vol. 51, no. 37, p. 375103, Sep. 2018.
- [15] Y. Azizi, M. Soleimani, and S. H. Sedighy, "Ultra-wideband radar cross section reduction using amplitude and phase gradient modulated surface," *Int. J. Appl. Phys.*, vol. 128, no. 20, p. 205301, Nov. 2020.
- [16] E. Kuester, M. Mohamed, M. Piket-May, and C. Holloway, "Averaged transition conditions for electromagnetic fields at a metafilm," *IEEE Trans. Antennas Propag.*, vol. 51, no. 10, pp. 2641–2651, Oct. 2003.
- [17] A. Epstein and G. V. Eleftheriades, "Huygens' metasurfaces via the equivalence principle: design and applications," *J. Opt. Soc. Am. B*, vol. 33, no. 2, p. A31, Feb. 2016.
- [18] Y. Ra'di and A. Alù, "Metagratings for efficient wavefront manipulation," *IEEE Photonics J.*, vol. 14, no. 1, pp. 1–13, Feb. 2022.
- [19] D. Sell, J. Yang, S. Doshay, R. Yang, and J. A. Fan, "Large-angle, multifunctional metagratings based on freeform multimode geometries," *Nano Lett.*, vol. 17, no. 6, pp. 3752–3757, Jun. 2017.
- [20] Y. Ra'di, D. L. Sounas, and A. Alù, "Metagratings: beyond the limits of graded metasurfaces for wave front control," *Phys. Rev. Lett.*, vol. 119, no. 6, p. 067404, Aug. 2017.
- [21] M. Memarian, X. Li, Y. Morimoto, and T. Itoh, "Wide-band/angle blazed surfaces using multiple coupled blazing resonances," *Sci. Rep.*, vol. 7, no. 1, p. 42286, Sep. 2017.
- [22] A. M. Wong and G. V. Eleftheriades, "Perfect anomalous reflection with a bipartite Huygens' metasurface," *Phys. Rev. X*, vol. 8, no. 1, p. 011036, Feb. 2018.
- [23] A. Epstein and O. Rabinovich, "Unveiling the properties of metagratings via a detailed analytical model for synthesis and analysis," *Phys. Rev. Appl.*, vol. 8, no. 5, Nov. 2017.
- [24] O. Rabinovich and A. Epstein, "Analytical design of printed circuit board (PCB) metagratings for perfect anomalous reflection," *IEEE Trans. Antennas Propag.*, vol. 66, no. 8, pp. 4086–4095, Aug. 2018.
- [25] O. Rabinovich, I. Kaplon, J. Reis, and A. Epstein, "Experimental demonstration and in-depth investigation of analytically designed anomalous reflection metagratings," *Phys. Rev. B*, vol. 99, no. 12, Mar. 2019.
- [26] O. Rabinovich and A. Epstein, "Arbitrary diffraction engineering with multilayered multielement metagratings," *IEEE Trans. Antennas Propag.*, vol. 68, no. 3, pp. 1553–1568, Mar. 2020.

- [27] —, “Nonradiative subdiffraction near-field patterns using metagratings,” *Appl. Phys. Lett.*, vol. 118, no. 13, p. 131105, Mar. 2021.
- [28] V. Popov, F. Boust, and S. N. Burokur, “Controlling diffraction patterns with metagratings,” *Phys. Rev. Appl.*, vol. 10, no. 1, p. 011002, Jul. 2018.
- [29] —, “Beamforming with metagratings at microwave frequencies: design procedure and experimental demonstration,” *IEEE Trans. Antennas Propag.*, vol. 68, no. 3, pp. 1533–1541, Mar. 2020.
- [30] A. Casolaro, A. Toscano, A. Alu, and F. Bilotti, “Dynamic beam steering with reconfigurable metagratings,” *IEEE Trans. Antennas Propag.*, vol. 68, no. 3, pp. 1542–1552, Mar. 2020.
- [31] V. Popov, B. Ratni, S. N. Burokur, and F. Boust, “Non-local reconfigurable sparse metasurface: efficient near-field and far-field wavefront manipulations,” *Adv. Opt. Mater.*, vol. 9, no. 4, p. 2001316, Feb. 2021.
- [32] G. Xu, G. V. Eleftheriades, and S. V. Hum, “Analysis and design of general printed circuit board metagratings with an equivalent circuit model approach,” *IEEE Trans. Antennas Propag.*, vol. 69, no. 8, pp. 4657–4669, Aug. 2021.
- [33] V. K. Killamsetty and A. Epstein, “Metagratings for perfect mode conversion in rectangular waveguides: theory and experiment,” *Phys. Rev. Appl.*, vol. 16, no. 1, p. 014038, Jul. 2021.
- [34] L. Biniashvili and A. Epstein, “Eliminating reflections in waveguide bends using a metagrating-inspired semianalytical methodology,” *IEEE Trans. Antennas Propag.*, vol. 70, no. 2, pp. 1221–1235, Feb. 2022.
- [35] V. Popov, S. N. Burokur, and F. Boust, “Conformal sparse metasurfaces for wavefront manipulation,” *Phys. Rev. Appl.*, vol. 14, no. 4, p. 044007, Oct. 2020.
- [36] G. Xu, V. G. Ataloglou, S. V. Hum, and G. V. Eleftheriades, “Extreme beam-forming with impedance metasurfaces featuring embedded sources and auxiliary surface wave optimization,” *IEEE Access*, vol. 10, pp. 28 670–28 684, 2022.
- [37] Y. Kerzhner and A. Epstein, “Metagrating-assisted high-directivity sparse antenna arrays for scanning applications,” *arXiv preprint arXiv:2206.00058*, May 2022.
- [38] V. Asadchy, A. Díaz-Rubio, S. Tsvetkova, D.-H. Kwon, A. Elsakka, M. Albooyeh, and S. Tretyakov, “Flat engineered multichannel reflectors,” *Phys. Rev. X*, vol. 7, no. 3, p. 031046, Sep. 2017.
- [39] Y. Yashno and A. Epstein, “Multichannel metagrating diffusers for broad-angle radar cross section (RCS) reduction,” in *Proc. IEEE Int. Symp. Antennas Propag. USNC-URSI Radio Sci. Meeting (APS/URSI)*, 2021, pp. 407–408.
- [40] X. Wang, A. Díaz-Rubio, and S. A. Tretyakov, “Independent control of multiple channels in metasurface devices,” *Phys. Rev. Appl.*, vol. 14, no. 2, Aug. 2020.
- [41] S. Tretyakov, *Analytical Modeling in Applied Electromagnetics*. Norwood, MA, USA: Artech House, 2003.
- [42] Y. Ra’di and A. Alù, “Reconfigurable metagratings,” *ACS Photonics*, vol. 5, no. 5, pp. 1779–1785, May 2018.
- [43] L.-Z. Yin, T.-J. Huang, F.-Y. Han, J.-Y. Liu, and P.-K. Liu, “Terahertz multichannel metasurfaces with sparse unit cells,” *Opt. Lett.*, vol. 44, no. 7, p. 1556, Apr. 2019.
- [44] A. Epstein, “Rigorous electromagnetic analysis of optical emission of organic light-emitting diodes,” Technion — Israel Institute of Technology, Haifa, Tech. Rep., 2013.
- [45] K. C. Gupta, R. Garg, I. Bahl, and P. Bhartia, *Microstrip Lines and Slotlines*. Norwood, MA, USA: Artech House., 1996.
- [46] David M. Pozar, *Microwave Engineering*. John Wiley & Sons, 2011.
- [47] O. Rabinovich and A. Epstein, “Dual-polarized all-metallic metagratings for perfect anomalous reflection,” *Phys. Rev. Appl.*, vol. 14, no. 6, p. 064028, Dec. 2020.
- [48] C. A. Balanis, *Advanced Engineering Electromagnetics*. Hoboken, NJ, USA: Wiley, 2012.
- [49] M. Chen, E. Abdo-Sánchez, A. Epstein, and G. V. Eleftheriades, “Theory, design, and experimental verification of a reflectionless bianisotropic Huygens’ metasurface for wide-angle refraction,” *Phys. Rev. B*, vol. 97, no. 12, p. 125433, Mar. 2018.
- [50] A. Díaz-Rubio, V. S. Asadchy, A. Elsakka, and S. A. Tretyakov, “From the generalized reflection law to the realization of perfect anomalous reflectors,” *Sci. Adv.*, vol. 3, no. 8, Aug. 2017.